ADVANCED FUNCTIONAL MATERIALS
www.afm-journal.de

4D Printed Shape Morphing Biocompatible Materials Based on Anisotropic Ferromagnetic Nanoparticles

*Tobias Kuhnt, Sandra Camarero-Espinosa, Milad Takhsha Ghahfarokhi, Mariana Arreguín, Riccardo Cabassi, Franca Albertini, Daniel Nieto, Matthew B. Baker, and Lorenzo Moroni**

Shape morphing materials, especially those fabricated by 4D printing, are gaining much attention due to their versatility of actuation and capability of being programmed in advance. These materials become particularly interesting for biomedical applications where implant materials could be remotely actuated, exerting a force on the surrounding tissues and cells. However, applications in this field have been restricted due to the biocompatibility of the materials and the character of the required stimuli, generally not compatible with physiological environments. Magnetic nanoparticles (MNPs) represent a great opportunity to this end; however, the actuation results in a uniform movement toward the magnet that requires anchoring of the object. Here, for the first time, the application of anisotropic Fe_3O_4 MNPs is described, and synthesized by a novel and easy route, that can be aligned on pre-defined patterns within objects printed by digital light processing, resulting in materials that can be actuated remotely (4D printing). These nanoparticles (178 nm × 55 nm), show good biocompatibility when directly seeded on top of human mesenchymal stem cells, despite being uptaken. Most importantly, the alignment of the MNPs can tune the movement of fabricated nanocomposite materials, resulting in complex movements of attraction or repulsion depending on the direction of the applied magnetic field.

1. Introduction

Shape morphing materials that can be triggered via external stimuli to actuate between different 3D shapes are of great interest as they can be used as soft robots or in healthcare and biomedicine applications among others.[1,2] Several external stimuli like heat, pH, ultrasounds, redox reactions, light, or magnetism have already been described.[3] Nonetheless, the use of magnetism seems to be very promising especially for biomedicine since the environment is often closed and confined, allowing control of the deformation of the material. Applications such as spatially controlled application of remotely triggered deformation or mechanical stimuli to host cells from an implanted material would certainly be of interest. Others, such as the implantation and removal of medical devices with complex architectures that can fold and unfold in situ would also profit from the development of such actuating systems. The use of magnetism has been proven to be safe and effective, especially in terms of response time. Magnetic actuators can lead to very fast response times and are very versatile in terms of changing frequencies or the intensity of the external magnetic field.[3f] The magnetic responsive structures that have been printed and used as examples for soft robots showcase these advantages.[4]

Two main types of magnetically responsive 4D printed structures have been reported so far in the literature and these are based on either ferromagnetic neodymium-iron-boron alloys (NdFeB) or superparamagnetic iron oxide nanoparticles (SPIONs). 4D structures based on NdFeB display a strong and fast response to magnetism. Some researchers have taken advantage of the ferromagnetic character of NdFeB nanoparticles to pattern movements within 4D structures with directional control. Thus, when the ferromagnets are aligned on defined orientations within the 4D structure, the application of magnetic fields results in a movement that can be unpaired (repulsion or attraction) in different areas of the same structure showing a controlled directionality and mechanical guidance.[2,4–5] Using this concept, Zhao and co-workers designed and fabricated extrusion-based 4D structures with predefined actuating patterns that allow them to fold and unfold as origami structures upon application of magnetic fields.[4] Hu et. al. further exploited this concept to create, by casting, soft robots with multimodal locomotion that owe their

T. Kuhnt, S. Camarero-Espinosa, M. Arreguín, D. Nieto, M. B. Baker, L. Moroni
Department of Complex Tissue Regeneration
MERLN Institute for Technology-Inspired Regenerative Medicine
Maastricht University
Universiteitssingel 40, 6229ER Maastricht, The Netherlands
E-mail: l.moroni@maastrichtuniversity.nl

T. Kuhnt, S. Camarero-Espinosa
POLYMAT
University of the Basque Country UPV/EHU
Avenida Tolosa 72, Donostia/San Sebastián, 20018 Gipuzkoa, Spain

S. Camarero-Espinosa
IKERBASQUE
Basque Foundation for Science
48009 Bilbao, Spain

M. Takhsha Ghahfarokhi, R. Cabassi, F. Albertini
Institute of Materials for Electronics and Magnetism (IMEM)
National Research Council (CNR)
Parco Area delle Scienze 37/A, 43124 Parma, Italy

The ORCID identification number(s) for the author(s) of this article can be found under https://doi.org/10.1002/adfm.202202539.

DOI: 10.1002/adfm.202202539

responsiveness to predefined orientations of embedded NdFeB ferromagnets.[2] Despite the great advantages shown by the use of NdFeB ferromagnets, their biocompatibility and biosafety still need to be proved, as preliminary studies point to moderate cytotoxicity of the alloy.[6]

The superparamagnetic nature of SPIONs results in particles that are magnetized under the influence of a given magnetic field.[7] In most cases, just a rotational or localized magnetization within the polymeric matrix is achieved.[8] Actuators based on iron oxide nanoparticles have a slower response to the magnetic field and, in the case of SPIONs, a lack of controlled directionality of the movement, unless the object is anchored in at least one of the extremes.[9] To overcome the limitations of the use of SPIONs in actuating structures some have combined them with thermally responsive shape-memory polymers. Thus, the application of a magnetic field results in heat that is transmitted to the polymer, inducing a change in the morphology.[10] The main advantage of actuating systems based on iron oxide is the biocompatibility of the nanoparticles.[11] In vitro studies have shown that there is a dependence of the cytotoxicity of the material with the dose, size, surface charge, and coating of the nanoparticles, being more cytotoxic with smaller sizes, higher doses (in the range of μg mL^{-1}) and uncoated particles.[11b] Moreover, in vivo studies show that intravenous or subcutaneous administration of iron oxide-based nanoparticles is safe up to doses of several gr per kg of the animal.[11a]

Iron oxide-based nanoparticles can be fabricated displaying different magnetic properties such as superparamagnetic (SPIONs), but also ferromagnetic. Anisotropic ferromagnetic nanoparticles have been reported in the literature, following long and dangerous synthesis routes that start from the fabrication of goethite, transformation into hematite, and further reduction to magnetite under H_2 atmosphere.[12] Here, we report on the two-step synthesis of anisotropic iron oxide MNPs by a co-precipitation method. On a first step, hematite is formed, to be later reduced into magnetite resulting in ferromagnetic nanoparticles. Moreover, the use of H_2 is avoided in the described process, avoiding this dangerous step. These elongated ferromagnetic particles show good biocompatibility when administrated directly to cells at up to a 0.5 mg mL^{-1} dose. When incorporated into biocompatible poly(caprolactone-co-trimethylcarbonate) urethane acrylate (PCTAc)[13] polymers and printed via DLP into stiff structures, their orientation can be tuned with the magnetic field, showing characteristic attraction or repulsion depending on the direction of the field. Further, the inclusion of these nanoparticles into softer, flexible, and actuable polyethylene oxide dimethacrylate (PEGDA) and subsequent DLP printing into anisotropic hydrogels with distinctly aligned MNPs patterns, allowed programming and actuating of the scaffolds with heterogeneous and complex movements.

2. Results and Discussion

2.1. Two-Step Synthesis of Anisotropic Magnetite Nanoparticles

Magnetite Fe_3O_4 nanoparticles have been synthesized traditionally as nanometric spheres with superparamagnetic properties.[7] Recently, rhombohedric, platelet, and needle-shaped magnetite nanoparticles with distinct magnetic behaviors were reported by Gavilán et al.[12b] Elongated, needle-like MNPs were prepared by a four-step synthesis route. This process involves the synthesis of goethite precursors by aerial oxidation, coating with SiO_2, dehydration into hematite, and final reduction into magnetite under H_2 atmosphere. Lately, this method was reviewed and optimized by Avolio et al. who showed that elongated magnetite nanoparticles behaved as ferromagnets.[12a]

In an attempt to simplify this synthesis route, we prepared elongated hematite nanoparticles following a protocol first described by Schurtenberger and co-workers (**Figure 1**a–g) that resulted in whisker-like nanoparticles of 210 ± 15 nm × 63 ± 6 nm dimensions (aspect ratio 3.4 ± 0.3).[14] X-ray diffraction analysis of the nanoparticles showed the characteristic diffraction peaks corresponding to the (012), (104), (110), (113), (024), (116), (018), (214), and (030) planes of hematite (Figure 1e). The nanoparticles also proved to be non-responsive upon application of a magnetic field (Figure 1g).

Elongated hematite nanoparticles were then reduced to magnetite nanoparticles that displayed ferromagnetic behavior. The nanoparticles, as obtained after the reduction step, accounted for an aspect ratio of 3.3 ± 0.5, with an average length of 178 ± 16 nm and a width of 55 ± 7 nm, slightly smaller than the hematite template due to the oxygen loss and the crystal re-organization. The formation of pores within the nanoparticles was also observed upon reduction, as previously described by others.[12] The recorded XRD patterns evidenced the formation of magnetite with the characteristic peaks corresponding to the (220), (311), (400), (422), (333), and (440) planes (Figure 1f). As expected, magnetite nanoparticles did respond to applied magnetic fields (Figure 1h).

2.2. Magnetic Characteristics of Anisotropic MNPs

Figure 2a shows the hysteresis loops of the MNPs as a function of the applied magnetic field at room temperature. The specific magnetization of the sample at $\mu_0 H_{max} = \pm 1.5$ T was obtained to be $|M| = 55.9$ Am^2 Kg^{-1}. Figure 2b shows a magnified version of the hysteresis loops from which the hysteretic character of the loops can be observed. The magnetic coercive field was obtained to be $\mu_0 H_C = 11$ mT and the remanent magnetization to be $Mr = 6.5$ Am^2 Kg^{-1}.

2.3. Response of Anisotropic MNPs to Magnetic Rotating Field

Micrometric-size agglomerated MNPs were made to spin by a tailored experimental set-up (**Figure 3**a). The particle of diameter ≈60 μm (Figure 3b) spinning in PBS under the action of a magnetic field rotating at a frequency of 100 Hz was recorded at different intensities of the applied field up to $H = 1.61$ mT (Figure 3c,d; Movies S1–S4, Supporting Information). The particle motion followed two different regime types, namely asynchronous and synchronous with the field, depending on the field intensity H.[15] For low applied H, the spinning frequency was well below the rotation frequency of H, so that it could still be discerned in real-time videos, and increased with H. For high applied intensities ($\mu_0 H = 1.28$ mT and higher (Figure 3c)), the spinning frequency became much higher than the frames-per-second

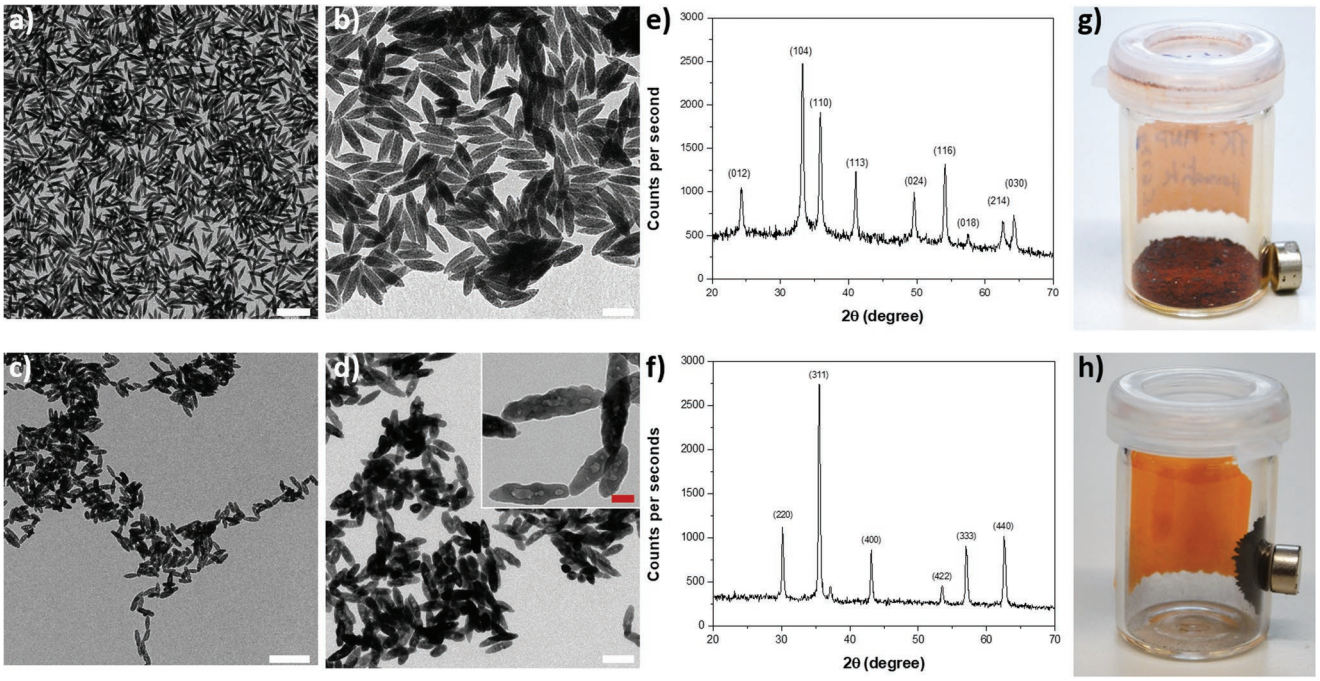

Figure 1. Synthesis of magnetite elongated MNPs from hematite templates. a,b) TEM images of hematite nanoparticles synthesized by co-precipitation showing an elongated shape. e) XRD pattern of hematite showing the characteristic diffraction peaks. g) hematite particles presented a red color and were not responsive to magnetic fields. c–d) TEM images of magnetite nanoparticles prepared by reduction of hematite templates in (a) and (b), showing the characteristic XRD spectra (f). Magnetite elongated nanoparticles were responsive to the applied magnetic fields and showed a black color (h). Scale bars are 500 nm in (a) and (c), 200 nm in (b) and (d), and 50 nm on the inset of (d), red scale bar. e) and f) present representative spectra; n = 3.

limit of the employed camera. Values of the spinning period as a function of H highlighted a power-law dependence (Figure 3d). Such behavior could be explained as the result of competition between the magnetic torque and the viscous friction acting on the particle, with $T = MH \sin \theta$ and $G = -8\pi\mu R^3\omega$ respectively for a spherical particle, where M is the particle magnetic dipole, H is the applied magnetic field, μ is the viscosity coefficient of the solvent, ω is the angular velocity and θ is the angular shift between the orientation of H and particle.

Numerical simulations of the system dynamics revealed that the spinning frequency in the high-field regime is the same of H, i.e. the particle follows synchronously the applied field possibly with a constant lag (Figure 3d inset). Simulations also showed that the transition between the two regimes takes place abruptly at a certain critical value of H, and that a similar transition could be observed as a function of the particle size and the applied frequency.

In summary, here we show a controlled spinning of the anisotropic MNPs by adjusting the applied magnetic field and frequency. This opens up the possibility of using an external rotating magnetic field as a mechanical trigger for transferring a controlled strain to the MNPs embedded in a hydrogel and the surrounding matrix.

2.4. Biocompatibility of MNPs

The biocompatibility of the MNPs was evaluated on human mesenchymal stem cells in a dose-dependent manner. Concentrations ranging from 0.05 to 5 mg mL^{-1} were added to the cell culture media and incubated for 4 and 24 h (**Figure 4**). The cells appeared to uptake the nanoparticles in a dose-dependent manner as observed by optical microscopy images where the concentration of nanoparticles associated with cells was clearly higher in 0.5 and 5 mg mL^{-1} concentrations after 24 h of culture (Figure 4a). To confirm the internalization of particles and rule out the adhesion of these to the surface of the cells, TEM images of hMSCs exposed to 5 mg mL^{-1} of MNPs were recorded after 4 and 24 h of incubation (Figure 4b–g). MNPs were phagocytized by hMSCs already after 4 h of culture, accumulating in the cytoplasm after 24 h of culture.

The toxicity of the uptaken MNPs was measured by means of released lactate dehydrogenase (LDH) to the culture medium after 4 and 24 h for all NMP concentrations (Figure 4h). The toxicity associated to the nanoparticle uptake was negligible after 4 h of culture, but increased after 24 h. Thus, after 24 h the LDH release showed a dose-dependent trend with 24 ± 10, 19 ±1, and 16 ± 4% of cytotoxicity. The LDH release and hence toxicity was associated to the intracellular concentration of Fe, which also increased with the incubation time from 11.3 ± 0.1 ng to 12.6 ±1 ng for samples exposed to the highest concentration and from 5.8 ± 2.6 to 8.8 ± 0.9 ng for the 0.5 mg mL^{-1} concentration (Figure 4i). At a concentration of 0.05 mg mL^{-1} the uptake was minimum for both time points with values that oscillated between 0.5 ± 0.2 and 0.2 ± 0.1 ng after 4 and 24 h, respectively.

However, the total amount of MNPs required to fabricate actuating scaffolds is much lower, and a burst release is not expected. For example, a typical 3D printed scaffold has a diameter of 6 mm, a height of 4 mm, and a (minimum) porosity of 50%, which translates in a volume of 5.6×10^{-8} m^3. Assuming

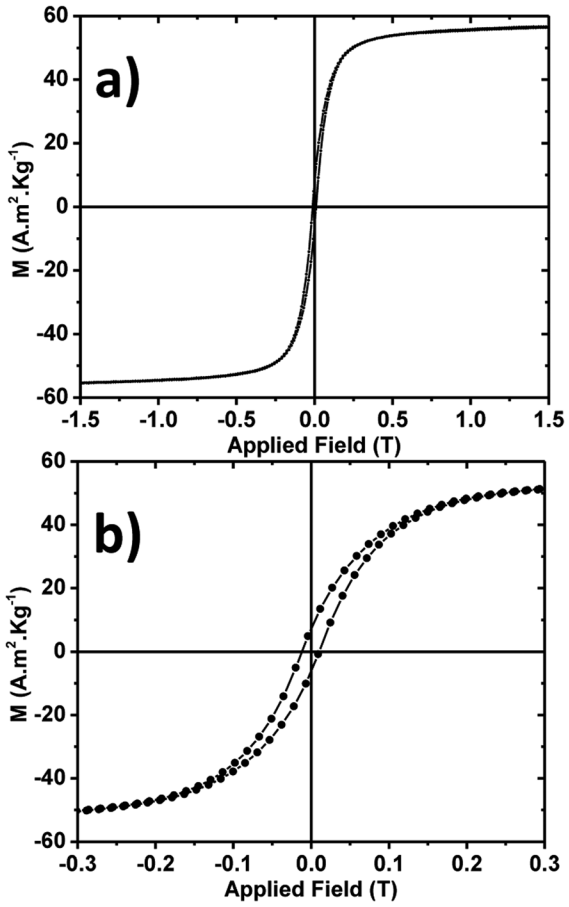

Figure 2. a) Hysteresis loops as a function of applied magnetic field $\mu_0 H = \pm 1.5$ T. b) Magnified version of (a) showing the magnetization curves in the field range $\mu_0 H = \pm 300$ mT. (a) and (b) display representative curves; n = 1.

a typical polymer density of 1.2 kg m^{-3}, the total weight of the scaffold is ≈67.8 mg and thus, the total load of nanoparticles would range from 0.67 to 3.4 mg for concentrations of 1 to 5 wt.%. To further confirm that hypothesis, and in a more realistic assay, human dermal fibroblast (HDFs) were cultured on top of PCTAc films fabricated by DLP and containing 5% of MNPs. After 24 h of culture, high cell viability was measured (>95%) (Figure 4j), confirming their applicability as fillers in nanocomposites for biological applications.

2.5. Control over the Orientation and Displacement of PCTAc Nanocomposites in Function of the MNP Alignment and the Magnetic Field

Having proven the applicability of the anisotropic MNPs at low concentrations as fillers in nanocomposites, we evaluated the magnetism of the particles when oriented in nanocomposite films, proving their ferromagnetic behavior. We used DLP printing to fabricate polymer nanocomposite films with embedded MNPs in the shape of compass needles (**Figure 5**). The embedded MNPs were oriented in the resin prior application of light by the application of a magnetic field to the vat. Thus, we fabricated compass needles with MNPs oriented along the long and short axes of the needles as well as perpendicularly to the thickness of the needles (Figure 5). Samples containing SPIONs were used as control. When the MNPs were oriented along the long axis of the compass needle, they could be attracted to the magnetic field moving in the direction of the particle orientation (Figure 5a). Switching the magnetic field from north to south (or vice versa) resulted in the repulsion of the needle that would rotate first, moving again on the direction of the long axes. Similarly, when MNPs were oriented along the short axes of the compass needles, they could be

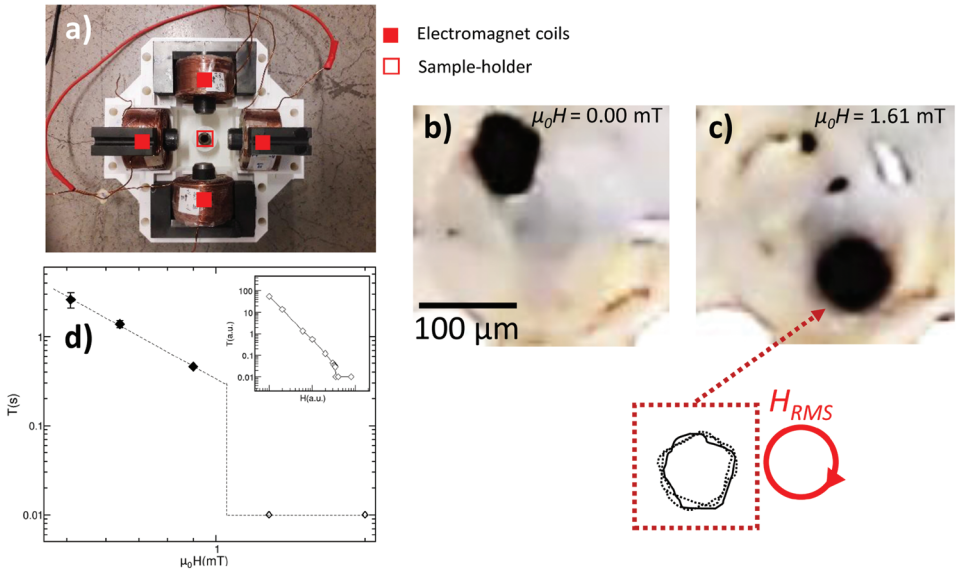

Figure 3. a) Experimental setup generating a magnetic field $H(t)$ rotating in the horizontal plane. b, c) Rotation of a ≈60 µm particle in PBS as a function of the applied magnetic field captured by an optical microscope. d) Rotation period of a ≈60 µm particle in PBS as a function of the applied magnetic field. n = 1 particle and data are presented as mean ± SD of measured rotations being a minimum of 7 for each data point. The dashed line is a guide for the eye to highlight the power low behavior and transition from asynchronous to the synchronous regime. Inset: results from numerical simulations showing the same type of behavior.

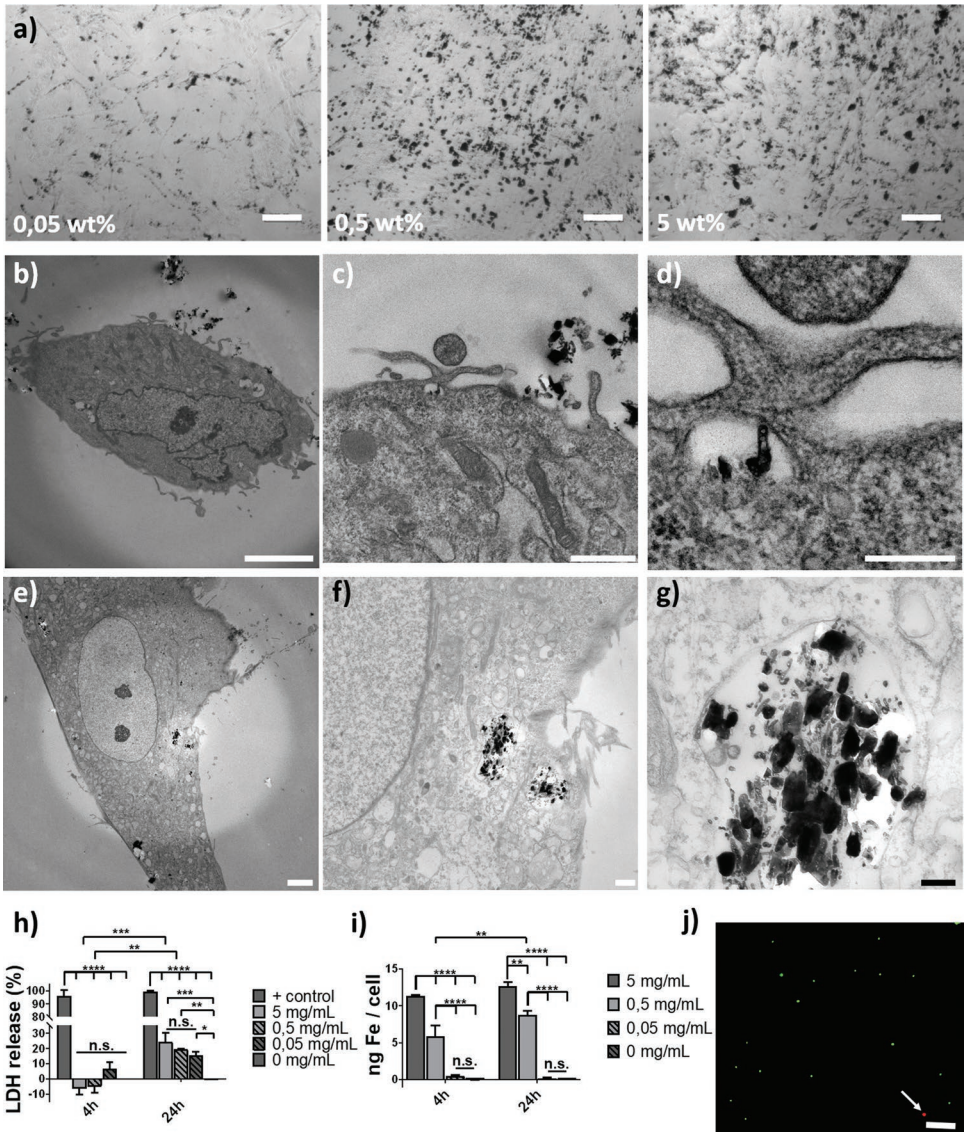

Figure 4. Biocompatibility of anisotropic MNPs and their composites. a) Optical microscopy images showing MNP uptake by hMSCs after 24 h of exposure to 5, 0.5 and 0.05 mg mL^{-1} MNP dispersions. Scale bar is 100 µm. b–g) TEM images of MNP uptake by hMSCs after 4 h b–d) and 24 h e–g) of exposure to 5 mg mL^{-1} nanoparticle dispersion. Images c) and d) and images f) and g) are magnification of b) and e), respectively. Scale bars are 5 µm b, e), 1 µm c, f) and 250 nm d, g). h) LDH release and Fe uptake i) of hMSCs exposed for 4 and 24 h to 5, 0.5 and 0.05 mg mL^{-1} of MNPs. j) Live (green)/dead (red) staining of HDFs cultured on PCTAc / MNP nanocomposited with 5 wt.% nanoparticle loading. Scale bar is 200 µm (j). Data is shown as mean ± SD, n = 3. Statistical significance was calculated using a two-way ANOVA test with a Sidak´s post-hoc multiple comparison test. For LDH release: interaction $F(4, 10) = 9.436$; $p = 0.002$; dose $F(4, 10) = 249.8$; $p < 0.0001$; time $F(1, 10) = 48.69$; $p < 0.0001$. For Fe concentrations: interaction $F(3, 8) = 5.88$; $p = 0.0202$; dose $F(3, 8) = 121.0$; $p < 0.0001$; time $F(1, 8) = 10.15$; $p = 0.0129$. P adjusted (****)$p < 0.0001$, (***)$p < 0.001$, (**)$p < 0.01$ and (*)$p < 0.1$.

attracted or repelled by the magnetic field with a simple switch of the orientation of the field and always moving in the direction of the short axis (Figure 5b). Alignment of the anisotropic MNPs perpendicularly to the thickness of the compass needles resulted in attraction/repulsion (depending on the direction of the field) of the needle irrespective of their orientation (Figure 5c). Finally, as control, we observed the displacement of compass needles with embedded SPIONs that showed completely different behavior. In the case of PCTAc/SPION compass needles, these were attracted towards the magnetic field irrespectively of its orientation and without previous alignment of the compass needle. Thus, these experiments showed a clear control over displacement, rotation, and orientation by the control of the alignment of the anisotropic ferromagnetic nanoparticles here synthesized.

2.6. Control over the Actuation of Polymer Nanocomposites in Function of the MNP Alignment

2.6.1. Optimization of hydrogels

To further control the actuation of nanocomposites we synthesized softer poly(ethylene glycol)diacrylate (PEGDA) light

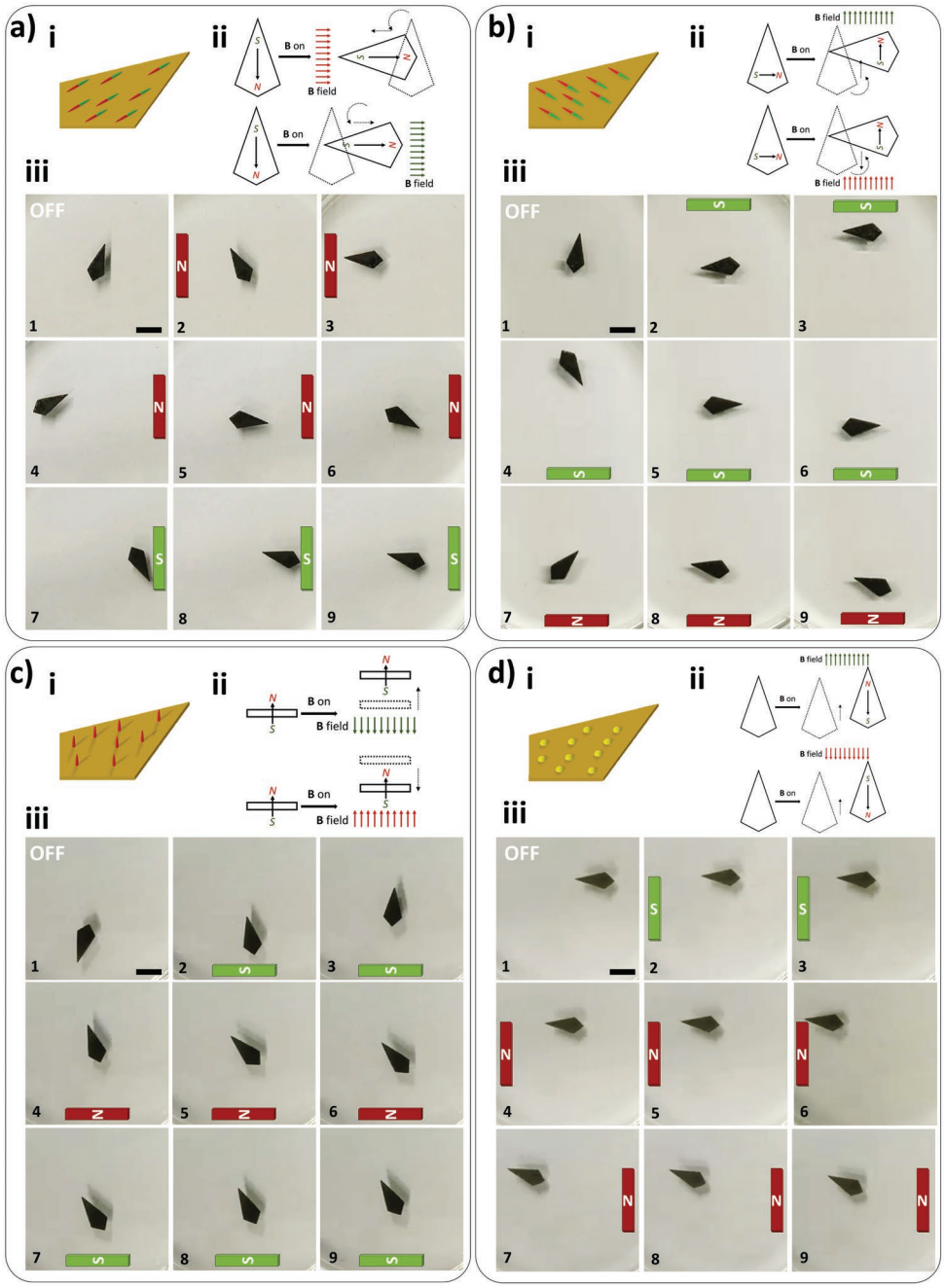

Figure 5. Directional control of movement and displacement by the orientation of MNPs in PCTAc nanocomposites. DLP printed PTCAc/MNPs compass needles with a) MNPs aligned along the long axis, b) along the short axis, c) perpendicularly to the thickness and d) with superparamagnetic nanoparticles (SPIONS) where no orientation is observed. i) Schematic representations of the alignment of MNPs inside the films and ii) designed rotation and displacement of the compass needles upon application of an external magnetic field. iii) Images taken from Movies S5–S8 (Supporting Information) following a time-lapse from right to left and top to bottom showing the actual response of the DLP printed compass needles. The scale bar is 1 cm in all images.

cross-linkable polymers that gave rise to more sensitive scaffolds (Figure S1, Supporting Information). We synthesized PEGDA with a starting PEG molecular weight (Mw) of 6 and 20 kDa and used them to prepare hydrogels with a 40% total solid content (**Figure 6**). Lower Mw hydrogels of 6 kDa resulted in the highest tensile Young's modulus (E)′ of 139 ± 6 kPa while the highest Mw of 20 kPa resulted in an E' of 1.57 ± 0.05 kPa (Figure 6a–b). The ultimate strain of the polymers was also dependent on the Mw, with an ultimate strain of 267 ± 67% and 893 ± 85% for 6 and 20 kDa polymers, respectively (Figure 6c). The hydrogels displayed an E´ and an ultimate strain with two orders of magnitude and 4 fold difference, respectively. Thus, we decided to evaluate intermediate compositions that allowed us to combine the high strain observed for 20 kDa polymers but with

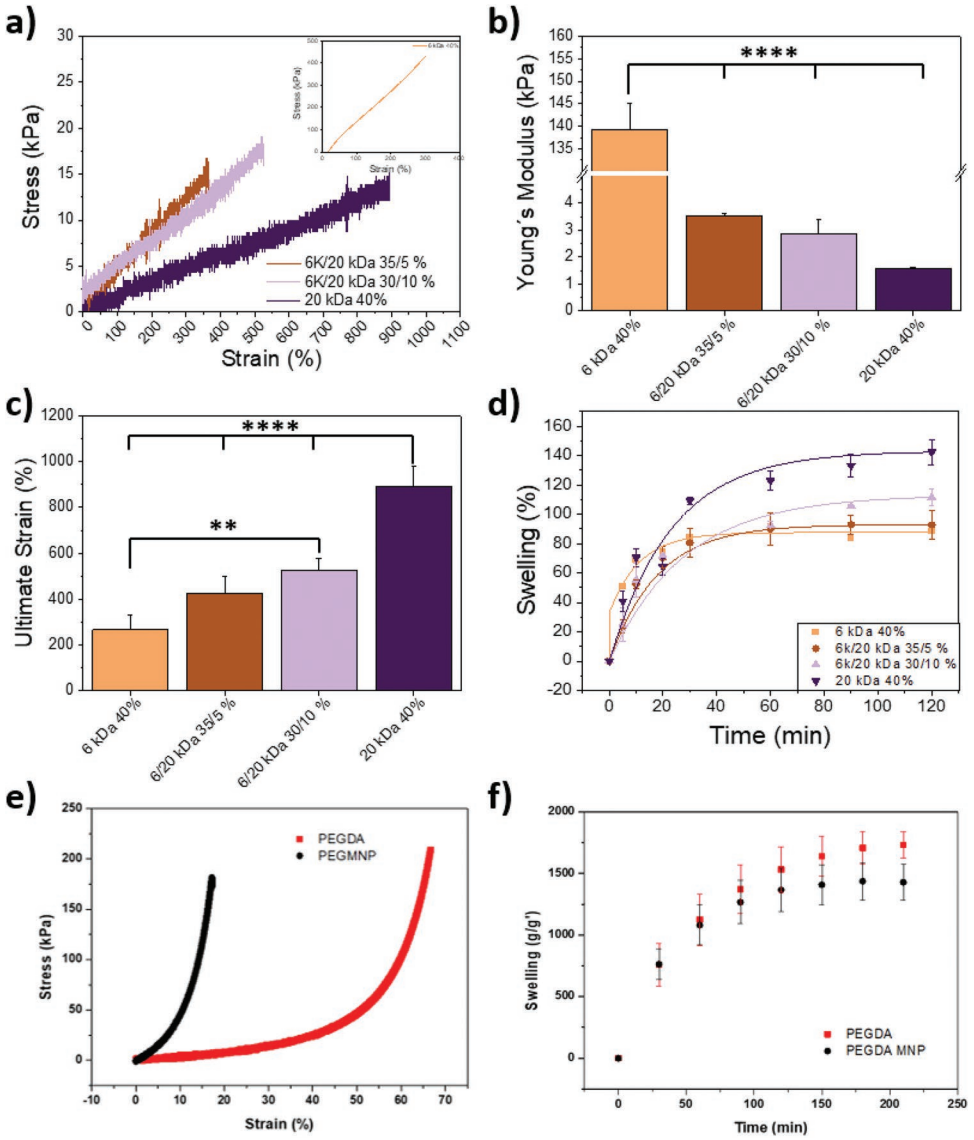

Figure 6. Mechanical properties and swelling behavior of PEGDA and PEGDA / MNP hydrogels. a) Representative tensile stress-strain curves of 6 kDa, 6/20 kDa 35/5%, 6/20 kDa 30/10%, and 20 kDa PEGDA blends. Inset shows the stress-strain curve of 6 kDa PEGDA. Young´s modulus (b) and ultimate strain (c) calculated from measurements in (a). d) Swelling ratio measured for the PEGDA hydrogels at 28 °C for 120 min of incubation. Representative compression stress-strain curves (e) and swelling ratios (f) measured for 6/20 kDa 35/5% PEGDA without and with (PEGMNP) 5 wt.% MNPs. Data in (b), (c), (d) and (f) is shown as mean ± SD; n = 3. (a) and (e) show representative curves; n = 3. Statistical significance was calculated using a one-way ANOVA test with a Tukey's post-hoc multiple comparison test. For Young´s Modulus: $F(3, 8) = 2215$; $p < 0.0001$. For ultimate strain: $F(3, 8) = 43.04$; $p < 0.0001$. P adjusted (****)$p < 0.0001$, (***)$p < 0.001$, (**)$p < 0.01$ and (*)$p < 0.1$.

a higher E'. Polymers containing a 35/5 and 30/10% ratio of 6 and 20 kDa PEGDA were prepared to retain the maximum solid content of 40%. These polymers, showed intermediate mechanical properties with values of E' of 3.51 ± 0.09 and 2.9 ± 0.5 kPa for 6/20 kPa 35/5% and 6/20 kPa 30/10%, respectively. The maximum strain measured was also intermediate to that of the single polymer hydrogels, with values of 428 ± 73% and 526 ± 51% for 6/20 kPa 35/5% and 6/20 kPa 30/10%, respectively.

Another important parameter for creating actuating 4D printed scaffolds was the swelling ratio of the polymers, as this would define the resolution of the printed structures. Therefore, we measured the swelling of the hydrogels in PBS at 28 °C, which reached a plateau after 2 h of incubation (Figure 6d). The swelling ratio measured was higher for samples containing a higher ratio of the high Mw PEGDA. These samples showed values of 140%, 110%, 93%, and 88% for 20 kDa, 6/20 kDa 30/10%, 6/20 kDa 35/5%, and 6 kDa polymers, respectively. Taking all these data together, we decided to use the 6/20 kDa 35/5% polymer blend as the optimal hydrogel composition for DLP printing.

To create actuating 4D printed hydrogels, we prepared 5 wt.% MNP dispersion in 6/20 kDa 35/5% PEGDA polymers, which resulted in hydrogel composites with higher E' under compression (Figure 6e) and a reduced swelling ratio (Figure 6f) when compared to neat 6/20 kDa 35/5% PEGDA hydrogels.

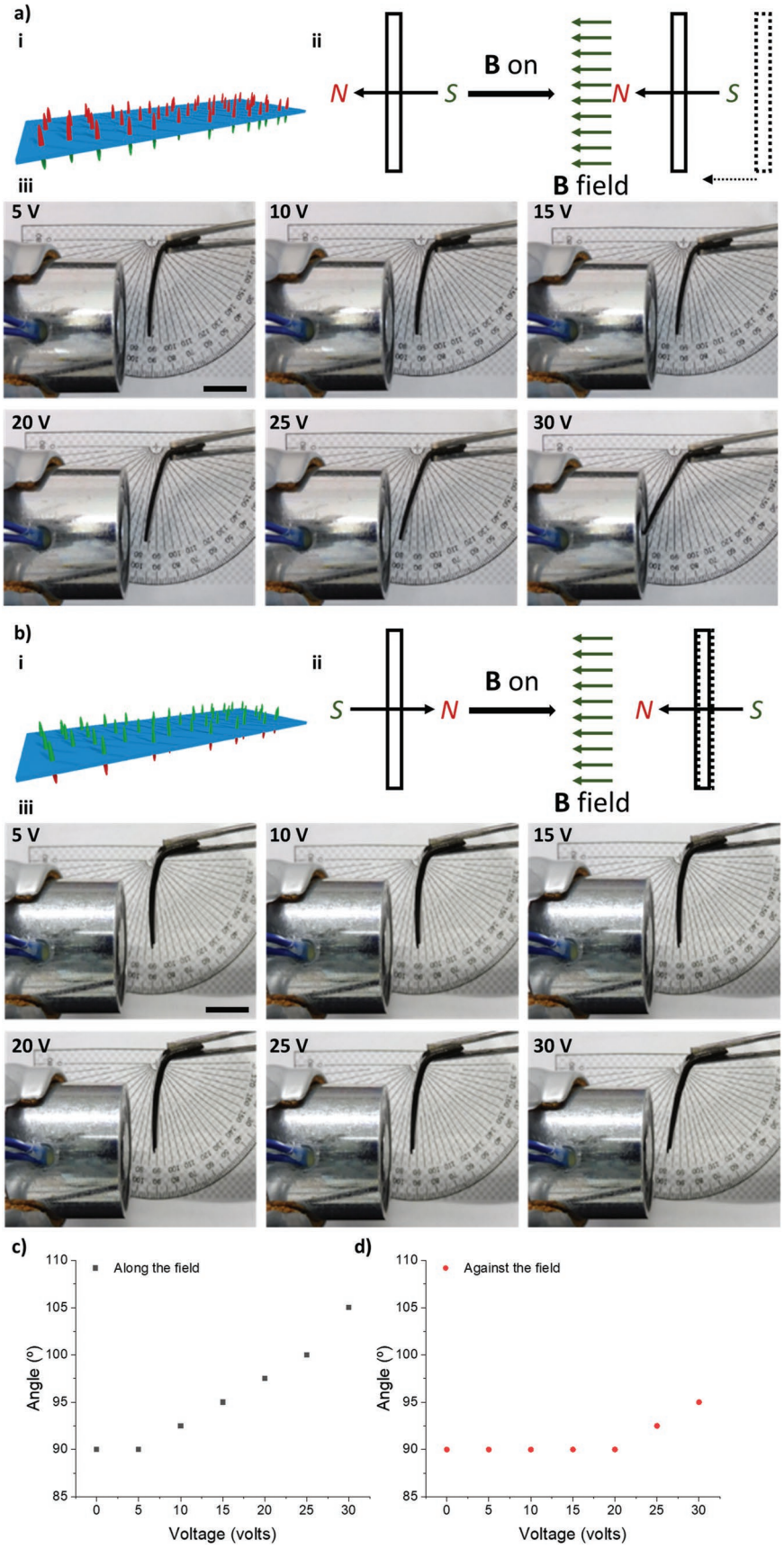

2.6.2. Controlled Actuation of PEGDA / MNP Nanocomposite Hydrogels

Next, we prepared PEGDA/5 wt.% MNP hydrogel films by DLP printing and varied the alignment of the anisotropic MNPs within the hydrogels (**Figure 7**) perpendicularly to the thickness of the film. Upon exposure to a varying magnetic field, the deflection of the films varied. Thus, when the MNPs were oriented parallel to the direction of the external field, they were attracted toward the electromagnet with a higher deflection as the voltage of the electromagnet was increased (Figure 7a and c). Contrary, when the particles were aligned antiparallel to the direction of the external field, the films showed no deflection until the current of the electromagnet was raised above 25 volts (Figure 7b and d). This exemplifies again the control of movement, rotation, and deflection that these anisotropic ferromagnetic nanoparticles are allowed to achieve in 4D printed scaffolds.

2.7. Unpaired Movement Control on Scaffolds with Distinct Areas of MNP Orientation

After proving the capability of the anisotropic MNPs to actuate nanocomposites with distinct orientational movements, we fabricated scaffolds with distinct areas of orientation to induce unpaired movements upon application of a magnetic field. As a model example, a 4D printed pair of hands were fabricated in which the left hand had non-oriented MNPs and the right hand had MNPs oriented along the length of the hand (**Figure 8**). Thus, when a magnetic field was applied, the random orientation of the MNPs resulted in a resting hand, while the hand with oriented MNPs moved towards the magnetic field, resulting in a waving hand (Movie S9, Supporting Information).

Finally, to demonstrate the fast and cyclic morphing capability of the actuating scaffolds, we printed PEGDA/5 wt.% MNPs hydrogels. We fabricated hollow structures with an inlet and an outlet, and filled them with liquid, mimicking a heart. These structures showed repeated actuation under the application of a magnetic field (Movie S10, Supporting Information).

3. Conclusion

We have shown a new synthetic route for the fabrication of anisotropic MNPs in a shorter and safer two-step method starting from hematite and without the use of hydrogen gas. Characterization via X-ray diffraction proved that the anisotropic MNPs account for the magnetite crystal structure. Most importantly, these novel MNPs are ferromagnetic, as proven by magnetization curves, which allowed us to create scaffolds with controlled shape-morphing properties. The MNPs could be internalized by hMSCs when exposed to high doses of up to 5 mg mL^{-1} showing minimal toxicity, negligible at lower and more realistic doses. When introduced into polymeric nanocomposites, human dermal fibroblasts cultured on top of the materials showed viability higher than 95%, proving again the exploitability of these MNPs and derived composites for biomedical applications. Control over the orientation of the MNPs within the DLP printed scaffolds allowed us to define the rotation, displacement, and deflection of the nanocomposites, without the need of anchoring them as it is the case for traditional superparamagnetic loaded composites. Moreover, we further showed that by carefully aligning the MNPs within distinct orientations in the same scaffold allows creating unpaired movements. Altogether, the fabrication of anisotropic ferromagnetic nanoparticles and their inclusion in DLP printed scaffolds allow us to pattern and control movements in 3D structures, which can be exploited in a variety of fields, including those of biomedicine and tissue engineering.

4. Experimental Section

Materials: All reagents and solvents were purchased from Sigma-Aldrich and used as received unless otherwise indicated.

MNP Co-Precipitation Process of Anisotropic Particles and SPIONs: Anisotropic MNPs were synthesized by the co-precipitation method of an iron salt following a protocol first established and then optimized by Schurtenberger and co-workers.[14] In brief, to obtain 2 g of magnetite anisotropic MNPs, 92.4 g of $Fe(ClO_4)_3{\cdot}6H_2O$ (200 mmol) were mixed with 1.3 g of $NaH_2PO_4{\cdot}H_2O$ (9.4 mmol), and 12 g of urea $(NH_2)_2CO$ (0.2 mol) in a 2 L glass bottle filled with distilled water and stirred until a homogeneous solution was obtained. The solution was then heated up to 100 °C in a preheated oven for 24 h. The day after, the particles appeared as brown sediment that was recovered by decanting the supernatant. Thereafter, the particles were washed in distilled water and recovered by centrifugation at 10.000 rpm for 10 min and decanting the supernatant. The washing process was repeated 3 times. Finally, the particles were left to dry in the oven at 100 °C. The formed hematite particles were then reduced to magnetite with stoichiometric amounts of titanium hydride. In brief, the hematite particles were placed together with the titanium hydride in a sintering oven and heated under a stream of nitrogen to 250 °C. The temperature was held for 5 min to remove all traces of moisture when the nitrogen stream was stopped. Then, the oven was heated up to 450 °C and kept for 6 h. After 6 h the initially red hematite particles turned into black magnetite particles.

SPIONs (magnetite, Figure S2, Supporting Information) nanoparticles were also synthesized by the co-precipitation method from two iron salts. In brief, 1 g of $FeCl_2{\cdot}4H_2O$ and 2 g of $FeCl_3$ was dissolved in 60 mL of distilled water under an N_2 atmosphere.

MNP Characterization: Nanoparticles were characterized morphologically by transmission electron microscopy (TEM) on a FEI/Tecnai G2 Spirit BioTWIN at a typical acceleration of 80 keV. Samples were prepared by casting a drop of a 0.1 wt.% dispersed MNPs in water on carbon-supported Cu grids. Crystallinity was measured using a Bruker X-ray diffractometer by directly depositing the MNP powder on a quartz holder. Spectra were recorded from 5 – 70 Θ angle.

Figure 7. Deflection control on PEGDA / MNP nanocomposites by alignment of the anisotropic MNPs. a) PEGDA / 5 wt.% MNPs hydrogel films where the nanoparticles were oriented perpendicular to the width of the film and in the direction of the field, showing deflection towards the magnet as the current of the electromagnet was increased (c). b) PEGDA / 5 wt.% MNPs hydrogel films where the nanoparticles were oriented perpendicular to the width of the film antiparallel to the direction of the magnetic field, showing unresponsiveness until the input voltage of the electromagnet was raised above 25 volts (d). i) Schematic representation of the alignment and orientation of the MNPs and ii) designed response to the external magnetic field. iii) Images were taken at a different input voltage of the electromagnet showing the response of the films. Scale bar is 1 cm in all images.

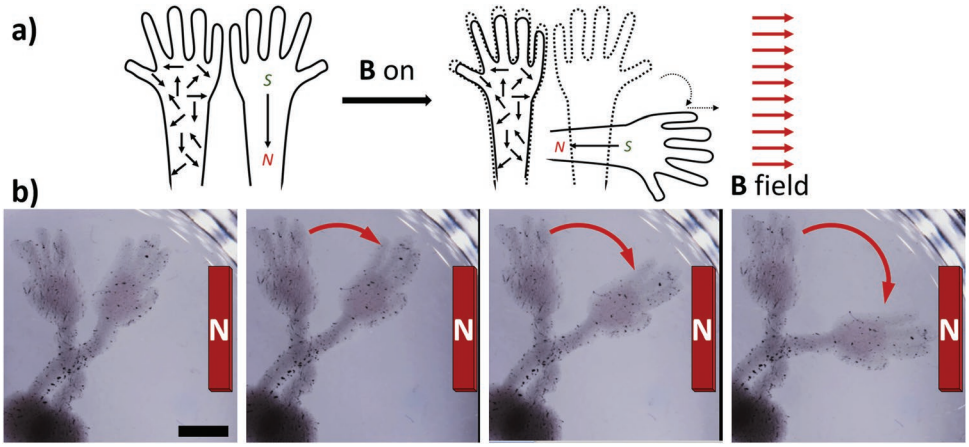

Figure 8. Unpaired movement of patterned 4D printed shape morphing hydrogels. a) Schematic representation of the designed scaffolds and magnetic response. b) PEGDA / 2 wt.% MNPs nanocomposite hydrogels were printed on the shape of hands having a distinct orientation. The left hand accounted for randomly oriented MNPs, which remain unresponsive to the magnetic field while the right hand, with MNPs oriented along the length of the hand, moves toward the magnetic field. The scale bar is 1 cm.

Magnetization of the MNPs was measured as a function of the external magnetic field at room temperature by a Vibrating Sample Magnetometer (VSM) model 7400 from Lake Shore (Westerville, USA) applying a magnetic field range of $\mu_0 H = \pm 1.5$ T.

The measurements in a rotating magnetic field were performed by the apparatus shown in Figure 3a. Two orthogonal coil-pairs have been connected to an AC wave form generator HP3245A supplying the two coil pairs with sinusoidal signals of the same frequency. The inductance of coils was enhanced by commercial E-shaped ferrite cores, obtaining an inductance $L = 32$ mH for each of the coil pairs. The coil pairs were connected in parallel to the AC generator output to provide the H_x and H_y components of the magnetic field, but different capacitances have been put in series to each coil pair, so to change the complex impedances Z_x and Z_y of two branches of the circuit. By choosing appropriate capacitance values, the impedances can provide equal modulus $Z_x = Z_y$ and phase shift of $\pi/2$: in this way, magnetic fields H(t) of constant strength rotating in the horizontal plane can be obtained. The appropriate capacitance values depend on the working frequency; for reasonable capacitances achievable with ordinary capacitors one can deal with frequencies in the order of hundreds of Hz, in particular we fixed a frequency of $f = 100$ Hz. Magnetic particles in a solution placed at the geometric center of the system could be seen to start spinning when the magnetic field was turned on as the resultant effect of magnetic torque and viscous friction acting on the particle. The rotation of a particle of diameter ≈60 µm was captured by an optical microscope (fps = 25) as a function of the applied magnetic field. The particle consists of the anisotropic MNPs aggregated naturally to form a micrometric-size particle.

Synthesis of Polymers: Poly(ethylene glycol) diacrylate (PEGDA, 6 kDa, and 20 kDa) was prepared according to well-established procedures.[16] In brief, to powder poly(ethylene glycol) a 2 molar excess of triethylamine and a 4 molar excess of acryloyl chloride were added in anhydrous dichloromethane and left stirring overnight under a nitrogen atmosphere.

Synthesis of PCTAc was done following a protocol previously described by us.[17] In brief, poly(caprolactone-co-trimethyl carbonate) prepolymers were synthesized by bulk ring opening polymerization using a 75:25 ratio of the monomers with stannous octanoate as catalyzer and triethylene glycol as initiator. After precipitation and washing steps, the prepolymers were end-capped with acrylated L-lysine isocyanate at 40 °C in dry toluene for 24 h.

Fabrication of Films and Scaffolds via DLP Printing: PTCAc and PCTAc /MNP films were prepared by mixing the resins in 2-(2-ethoxyethoxy)ethyl acrylate (EOEOEA) at 70 wt.%. To these dissolutions a 5 wt.% of MNPs were added to create nanocomposites and manually mixed to obtain a homogeneous resin. Resins were added to the polymerization vat together with 1 wt.% of triphenylphosphine oxide (TPO) as an initiator.

PEGDA 6 kDa 40 wt.%, 20 kDa 40 wt.%, 6/20 kDa 35/5 wt.%, 6/20 kDa 30/10 wt.%, and 6/20 kDa 35/5 wt.% in water with 5 wt.% MNPs were printed as films and scaffolds by directly adding the dissolution to the polymerization vat and adding 0.5 wt.% lithium phenyl-2,4,6-trimethylbenzoylphosphinate (LAP) as a photoinitiator.

All polymer films were printed using a DLP (ARM 10, Roland, Geel, Belgium). Hydrogel scaffolds were printed using a custom made DLP bioprinter equiped with a Wintech DLP PRO6500 projector (PRO6500 utilizes Texas Instrument's 0.65″ 1080p digital mirror device, DMD), a 385 nm UV light source (1100 mW), UV coated optical lenses and a high resolution (20 nm) Z platform.

Mechanical Properties: Samples for mechanical analysis were prepared as printed cylinders of 0.5 cm diameter and 0.5 cm height. For tensile tests, films were printed on the shape of flat dumbbells with test areas of 0.5 cm in width by 1 cm in length. All samples were tested using a TA ElectroForce (TA Instruments) mechanical tester equipped with a 4.5 N load cell. Tests were conducted at a strain rate of 0.1 mm s^{-1} and samples were run in triplicate.

Cell Culture and Biocompatibility Analysis: Human mesenchymal stem cells were obtained from the Texas A&M College of Medicine's Institute for Regenerative Medicine where cells were isolated from a 22-year old donor by aspiration and after written consent by the donor and ethical approval from the local and national authorities. Cells at passage 0 were expanded until passage 4. In brief, cells were seeded at a density of 1000 cell cm^{-2} and cultured in α-MEM supplemented with Glutamax (Gibco) and 10% fetal bovine serum (FBS, Sigma-Aldrich). Cells in passage 5 were used for the biocompatibility experiments.

For LDH and Fe content experiments, cells were plated at a density of 5.000 cell cm^{-2} in 24 well-plates and let adhere for 24 h. After 24 h, the media was changed to complete media dispersions with 0, 0.05, 0.5, or 5 mg Ml^{-1} of added MNPs. After 4 and 24 h, the samples' media was collected for LDH measurements and centrifuged at 5000 rpm for 10 min to remove any MNP. The clean medium was transferred to new centrifugation tubes and kept at –40 °C until use. LDH content was measured following the indications of the producer (Cyquant LDH cytotoxicity assay, ThermoFisher). The attached cells were then washed 5 times with phosphate buffer saline (PBS) to remove any excess particles and Fe content measured by the Prussian Blue colorimetric assay as previously described by others.[18] In brief, 100 µL of various concentrations of MNPs were dissolved for 1 h in 6 N HCl to create a standard curve. The cell samples were also digested using 6 N HCl. 50 µL of each dissolution, sample, and standards were added per well

in a 96-well plate. To these, 50 µL of 5% $K_4[Fe(CN)_6]$ were added and the absorbance was then determined at a wavelength of 690 nm.

For TEM studies, cells were seeded at 5000 cell cm^{-2} on top of thin polystyrene (PS) films previously sterilized with 70% ethanol and inserted in 6 well-plates. After 4 and 24 h of exposure to MNPs as described above, the media was removed and the cells were washed 5 times with PBS. Then, cells were fixed with 4% paraformaldehyde for 15 min and rinsed again with PBS. PS supported cell monolayers were then attached to an Epon LX112 resin (Hexion) stub from which samples were sliced on an ultra-cryomicrotome Leica EM FC6. The samples were collected on TEM carbon-supported Cu grids and observed under an FEI/Tecnai G2 Spirit BioTWIN microscope. For cell viability studies, human dermal fibroblast (HDF, CC-2511 from Lonza) were seeded at 10.000 cell cm-2 on top of the films previously sterilised in 70% ethanol and cultured on a medium composed of basal medium (CC-3131, Lonza), supplements (CC-4126, Lonza) and gentamicin sulfate-amphotericin (GA-1000, Lonza). After 24h of seeding, cells were stained with calcein/ethidium bromide homodimer Live/Dead staining kit (Thermofisher), following manufacturer instructions, and visualized under a Nikon Eclipse Ti, equipped with Ander Zyla sCMOS camera.

Scaffold and Film Actuation: Actuation of samples under wet conditions, e.g., compass needles and waving hands, was done by simply approaching manually a nickel-plated NdFeB magnet with a strength of 25 kg (≈245 N) and a displacement force of 5 kg (≈49 N) (Q-40-20-10-N, Supermagnete). Samples under dry conditions, e.g. hydrogel deflecting films and heart-like structures, were actuated by activating an electromagnet (ITS-MS-3025-12VDC, Intertec Components) with a holding power of 100 N.

Statistical Analysis: Raw data was analyzed as recorded without pre-processing. Data was presented as mean ± SD in all experiments, with a sample size of n = 3. Statistical significance of mechanical data, e.g. Young's moduli and ultimate strain was calculated using one-way ANOVA with a Tukey's post-hoc multiple comparison test. Statistical significance of LDH release and Fe uptake were calculated using a two-way ANOVA test with a Sidak's post-hoc multiple comparison test. All statistical analysis were carried out using GraphPad Prism 8.

Supporting Information

Supporting Information is available from the Wiley Online Library or from the author.

Acknowledgements

T.K., and S.C.-E. contributed equally to this work. This work was supported financially by the Province of Limburg and the Brightlands Materials Center. The authors were also grateful to the research program Innovation Fund Chemistry, which was partly financed by the Netherlands Organization for Scientific Research (NWO) under TA grant agreement 731.016.202 ("DynAM"). The authors acknowledge the Texas A&M Health Science Center College of Medicine Institute for Regenerative Medicine at Scott & White who isolated and provided the cells through a grant from NCRR of the NIH (Grant #P40RR017447).

Conflict of Interest

The authors declare no conflict of interest.

Data Availability Statement

The data that support the findings of this study are available from the corresponding author upon reasonable request.

Keywords

4D printing, anisotropic, biocompatible, magnetic nanoparticles, shape morphing

Received: March 4, 2022
Revised: April 26, 2022
Published online: June 11, 2022

[1] E. Yarali, M. Baniasadi, A. Zolfagharian, M. Chavoshi, F. Arefi, M. Hossain, A. Bastola, M. Ansari, A. Foyouzat, A. Dabbagh, M. Ebrahimi, M. J. Mirzaali, M. Bodaghi, *Appl. Mater. Today* **2022**, *26*, 101306.
[2] W. Q. Hu, G. Z. Lum, M. Mastrangeli, M. Sitti, *Nature* **2018**, *554*, 81.
[3] a) A. S. Gladman, E. A. Matsumoto, R. G. Nuzzo, L. Mahadevan, J. A. Lewis, *Nat. Mater.* **2016**, *15*, 413; b) S. Camarero-Espinosa, L. Moroni, *Nat. Commun.* **2021**, *12*, 1031; c) X. Kuang, D. J. Roach, J. T. Wu, C. M. Hamel, Z. Ding, T. J. Wang, M. L. Dunn, H. J. Qi, *Adv. Funct. Mater.* **2019**, 29; d) A. Kotikian, R. L. Truby, J. W. Boley, T. J. White, J. A. Lewis, *Adv. Mater.* **2018**, *30*, 1706164; e) M. Schaffner, J. A. Faber, L. Pianegonda, P. A. Rühs, F. Coulter, A. R. Studart, *Nat. Commun.* **2018**, *9*, 878; f) Q. Ze, X. Kuang, S. Wu, J. Wong, S. M. Montgomery, R. Zhang, J. M. Kovitz, F. Yang, H. J. Qi, R. Zhao, *Adv. Mater.* **2020**, *32*, 1906657.
[4] Y. Kim, H. Yuk, R. Zhao, S. A. Chester, X. Zhao, *Nature* **2018**, *558*, 274.
[5] H. Zhu, Y. He, Y. Wang, Y. Zhao, C. Jiang, *Adv. Intell. Syst.* **2022**, *4*, 2100137.
[6] a) V. E. Donohue, F. McDonald, R. Evans, *J Appl Biomater* **1995**, *6*, 69; b) M. Hopp, S. Rogaschewski, T. Groth, *J. Mater. Sci.: Mater. Med.* **2003**, *14*, 335.
[7] A. K. Gupta, M. Gupta, *Biomaterials* **2005**, *26*, 3995.
[8] a) M. Khalili, H. Keshvari, R. Imani, A. N. Sohi, E. Esmaeili, M. Tajabadi, *Polym. Adv. Technol.* **2022**, *33*, 782; b) C. Shuai, W. Yang, C. He, S. Peng, C. Gao, Y. Yang, F. Qi, P. Feng, *Mater. Des.* **2020**, *185*, 108275; c) J.-J. Kim, R. K. Singh, S.-J. Seo, T.-H. Kim, J.-H. Kim, E.-J. Lee, H.-W. Kim, *RSC Adv.* **2014**, *4*, 17325.
[9] J. Spangenberg, D. Kilian, C. Czichy, T. Ahlfeld, A. Lode, S. Günther, S. Odenbach, M. Gelinsky, *ACS Biomater. Sci. Eng.* **2021**, *7*, 648.
[10] F. Zhang, L. Wang, Z. Zheng, Y. Liu, J. Leng, *Composites, Part A* **2019**, *125*, 105571.
[11] a) L. H. Reddy, J. L. Arias, J. Nicolas, P. Couvreur, *Chem. Rev.* **2012**, *112*, 5818; b) V. Valdiglesias, N. Fernández-Bertólez, G. Kiliç, C. Costa, S. Costa, S. Fraga, M. J. Bessa, E. Pásaro, J. P. Teixeira, B. Laffon, *J. Trace. Elem. Med. Biol.* **2016**, *38*, 53.
[12] a) M. Avolio, H. Gavilán, E. Mazario, F. Brero, P. Arosio, A. Lascialfari, M. Puerto Morales, *Phys. Chem. Chem. Phys.* **2019**, *21*, 18741; b) H. Gavilán, O. Posth, L. K. Bogart, U. Steinhoff, L. Gutiérrez, M. P. Morales, *Acta Mater.* **2017**, *125*, 416.
[13] T. Kuhnt, R. Marroquin Garcia, S. Camarero-Espinosa, A. Dias, A. T. Ten Cate, C. A. van Blitterswijk, L. Moroni, M. B. Baker, *Biomater. Sci.* **2019**, *7*, 4984.
[14] a) I. Martchenko, J. J. Crassous, A. M. Mihut, E. Bialik, A. M. Hirt, C. Rufier, A. Menzel, H. Dietsch, P. Linse, P. Schurtenberger, *Soft Matter* **2016**, *12*, 8755; b) C. Rufier, M. Reufer, H. Dietsch, P. Schurtenberger, *Langmuir* **2011**, *27*, 6622.
[15] S. Bhat, T. P. Kurzweg, A. Guez, G. Friedman, *Appl. Phys. Lett.* **2009**, *94*, 224105.
[16] B. Grigoryan, S. J. Paulsen, D. C. Corbett, D. W. Sazer, C. L. Fortin, A. J. Zaita, P. T. Greenfield, N. J. Calafat, J. P. Gounley, A. H. Ta, F. Johansson, A. Randles, J. E. Rosenkrantz, J. D. Louis-Rosenberg, P. A. Galie, K. R. Stevens, J. S. Miller, *Science* **2019**, *364*, 458.
[17] T. Kuhnt, R. Marroquín García, S. Camarero-Espinosa, A. Dias, A. T. ten Cate, C. A. van Blitterswijk, L. Moroni, M. B. Baker, *Biomater. Sci.* **2019**, *7*, 4984.
[18] V. Hirsch, C. Kinnear, M. Moniatte, B. Rothen-Rutishauser, M. J. D. Clift, A. Fink, *Nanoscale* **2013**, *5*, 3723.